Orbital Verification of the CXO High Resolution Mirror Assembly Alignment and Vignetting

T. J. Gaetz[a], D. Jerius[a], R. J. Edgar[a], L. Van Speybroeck[a],
D. A. Schwartz[a], M. L. Markevitch[a],

and

S. C. Taylor[b], N. S. Schulz[b]

[a]Harvard-Smithsonian Center for Astrophysics, Cambridge, MA 02138 USA

[b]MIT Center for Space Research, Cambridge, MA 02139 USA

ABSTRACT

Prior to launch, the High Resolution Mirror Assembly (HRMA) of the *Chandra X-ray Observatory* underwent extensive ground testing at the X-ray Calibration Facility (XRCF) at the Marshall Space Flight Center in Huntsville, Alabama. The resulting data were used to validate a high fidelity raytrace model for the HRMA performance. Further observations made during the post-launch Orbital Activation and Calibration period allow the on-orbit condition of the X-ray optics to be assessed.

Based on these ground-based and on-orbit data, we examine the alignment of the X-ray optics based on the off-axis point spread function. We discuss how single-reflection ghost data obtained at XRCF can be used to better constrain the HRMA optical axis data. We examine the vignetting and the single-reflection ghost suppression properties of the telescope. Slight imperfections in alignment lead to a small azimuthal dependence of the off-axis effective area; the morphology of off-axis images also shows an additional small azimuthal dependence varying as 1/2 the position angle.

Keywords: X-ray optics, alignment, vignetting, *Chandra*, CXO

1. INTRODUCTION

The imaging performance of the *Chandra X-Ray Observatory* (*CXO*) depends critically upon the alignment of the mirrors in its High Resolution Mirror Assembly (HRMA). The HRMA consists of four nested Wolter Type-I mirror pairs; each mirror pair consists of a paraboloid (P) mirror and a matching hyperboloid (H) mirror; for historical reasons the mirror pairs (or shells) are numbered (largest to smallest) 1, 3, 4, and 6.

HRMA alignment measurements were performed during HRMA construction at Eastman Kodak Company (EKC), Rochester, New York. Ground calibration of the completed HRMA was performed at the X-ray Calibration Facility (XRCF) at the Marshall Space Flight Center, Huntsville, Alabama; see Ref. 1 for an overview. Finally, calibration measurements were obtained during the *Chandra* Orbital Activation and Calibration during the first two months of operation.

Ground calibration at the XRCF allowed assessment of the individual mirror pairs using monochromatic X-ray sources, but ground testing artifacts such as finite source distance and gravity-induced distortions had to be backed out using a model. On-orbit calibration did not have the latter problems, but provides information primarily on the HRMA as a whole, with limited access to individual mirror properties. In addition, limited knowledge of the absolute spatial and spectral properties of cosmic sources limits the types of calibration experiments which can be

Send correspondence to TJG; E-mail: gaetz@head.cfa.harvard.edu

performed. Because of the limited ground calibration time available and limitations of on-orbit calibration, the goal of the HRMA calibration is the validation of a high fidelity raytrace model of the HRMA performance; the raytrace model can then be used to interpolate (or extrapolate) the performance based on the available calibration data.

The raytrace model is based on the raytrace suite `SAOsac`. Beginning with the original mirror prescription (adjusted for end-cuts), we add low-frequency figure errors based on mirror metrology, axial spacings based on measurements performed during HRMA buildup, baffle dimensions and locations based on measurements or design, and misalignments of the optics (see §2). Scattering due to mirror microroughness is included statistically using a surface scattering model based on the mirror metrology. The mirror reflectivities are modeled using a multilayer reflection model including "roughness" with inputs derived from detailed optical constants for Iridium based on synchrotron measurements.[2]

For the on-orbit simulations presented here, we used the `orbit_XRCF+tilts_01.cnf` configuration of the raytrace model; it includes the 19990219 version of the optical constants, the `HDOS_980623` version of the microscatter tables, and the `EKCHDOS06` version of the HRMA alignment model (modified by an additional shell 6 tile; see §2). A $0\farcs25$ FWHM Gaussian blur was applied to simulate the aspect blur. We projected to the detector planes and applied the detector response using version 2.22 of `MARX`.[3]

Revised versions of optical constants and microscattering are currently undergoing testing; because we scale the off-axis effective area to the on-axis values, there should be little effect on the results presented here. An updated HRMA alignment model is in progress; preliminary indications are that the magnitude of the coma-compensated decenters remain about the same (see §2), but the directions may be revised towards the Z-axis. This would slightly change the direction of the off-axis vignetting asymmetries in §6.

2. HRMA ALIGNMENT — SUMMARY

During HRMA buildup at Eastman Kodak Company (EKC), the alignment state of the HRMA optics was assessed and monitored using the EKC HRMA Alignment Test System (HATS). In this configuration the HRMA optics were supported vertically in an assembly and testing tower (H optics upper, P optics lower) suspended above an Autocollimating Flat (ACF). The alignment test was basically a double-pass Hartmann test of the X-ray optics; the variation in the return beam centroid location with azimuth around the optic was used to assess the on-axis coma and parfocalization of the system. For a given mirror pair, the HATS measured the double-pass centroids for a set of 24 apertures equally spaced in azimuth around the optic. The centroids of the returned beam were Fourier transformed and the low-order terms interpreted in terms of rigid-body misalignments (coma, lateral parfocalization, and axial parfocalization); in addition, 2nd and 3rd order assembly strains (assessed from the 3rd and 4th order Fourier coefficients) were incorporated into the raytrace model.

X-ray testing of HMRA was conducted at the X-ray Calibration Facility (XRCF) at the Marshall Space Flight Center in Huntsville, Alabama. The X-ray source was at a distance of approximately 527.3 m from the HRMA CAP. In the alignment tests, the on-axis coma and axial parfocalization were measured using a system of quadrant shutters which allowed any combination of individual quadrants of individual mirror pairs to be isolated. The centroid of the focused beam was determined by using a flow proportional counter and moveable pinholes to map out the focused X-ray beam.

Because of the presence of a number of axially symmetric biases in the optical measurements (including deformations under load, curvature of the ACF, sampling of the "dimples" induced by the mirror supports under 1g, and refraction by radial air temperature gradients within the HRMA), the optically determined axial parfocalization values are considered to be less accurate than those obtained from the X-ray ground calibration.

During the ground X-ray calibration, other measurements indicated the presence of an internal misalignment within the HRMA: the H mirrors are offset from the P mirrors by $\sim 450\,\mu$m, but with compensating tilts so that the mirror decenters do not result in additional coma at the focal plane (*i.e.* a coma-compensated decenter). The effects were originally seen during the attempts to determine the X-ray optical axis (see §3). The misalignment was fully diagnosed and characterized (Ref. 4) using off-axis images taken with the High-Speed Imager (HSI, a microchannel-plate detector).

Finally, a deep exposure taken ~ 9.7 mm out of focus indicated a slight offset in the image from P_6H_6 relative to the other mirror pairs. We have tentatively identified this as a mirror tilt component, but it is could also be the result of a mirror deformation or a small HRMA tilt. We use the EKCHDOS06 mirror alignment parameters, but with an added $0\farcs1$ internal tilt for mirror pair 6.

The resulting mirror alignment parameters in the AXAF coordinate system are listed in Table 1. Combined with cone-angle corrections, these result in the parfocalization and on-axis coma values listed in Table 2.

Table 1. Mirror Body Center Coordinates (AXAF coordinate system)

Mirror	X (mm)	Y (mm)	Z (mm)	θ_Y ($''$)	θ_Z ($''$)
P_1	426.5761	0.12390	−0.2151	0.000000	0.000000
P_3	436.7098	0.08675	−0.2437	0.000000	0.000000
P_4	440.3572	0.08634	−0.2168	0.000000	0.000000
P_6	445.0821	0.08625	−0.2245	0.000000	0.050000
H_1	−481.0146	−0.11540	0.2060	−4.445448	−2.419413
H_3	−480.9282	−0.08365	0.2345	−4.994325	−1.854230
H_4	−480.8279	−0.08386	0.2065	−4.435027	−1.846808
H_6	−479.2152	−0.10960	0.2067	−4.489191	−2.422057

Table 2. Misalignments (at focal plane) (AXAF coordinate system)

Mirror	ΔX (μm)	ΔY (μm)	ΔZ (μm)	Coma Y ($''$)	Coma Z ($''$)
MP_1	−42	−3.00	−0.86	−0.0902	0.0293
MP_3	0	2.65	2.05	0.0672	−0.0207
MP_4	277	2.08	0.28	0.0619	−0.0042
MP_6	−174	0.84	−2.22	0.4186	−0.0329

We use "AXAF coordinates"; in this system, the X–axis is the optical axis with X increasing from the detector towards the X-ray mirrors. The Z–axis is the anti-sunward direction, and the Y–axis is in the grating dispersion direction, completing a right-handed coordinate system. (Note that the "XRCF" system used by Ref. 4 is rotated 180° about the X–axis relative to the "AXAF" system used here.) The coordinate origin is taken to be coincident with the intersection of the nominal optical axis with the plane defined by the P side of the HRMA Central Aperture Plate (CAP datum –A–), 18.15 mm forward of the nominal HRMA node. (The CAP is the major structural support plate between the P and H optics.) θ_Y and θ_Z are positive rotations about axes parallel to the $+Y$ and $+Z$ axes, respectively.

3. OPTICAL AXIS

For an ideal system, the axisymmetry of the HRMA would imply that the optical axis coincides with the symmetry axis. Because of mirror deformations and internal misalignments, the choice of axis is no longer unique. For a point source at infinity, the optical axis could be defined in a number of ways, including: the angle at which the effective area peaks, the angle at which the size of the Point Spread Function (PSF) is minimized according to some metric, or the angle at which the PSF ellipticity is minimum.

Off-axis angles are specified by spherical polar angles θ, measured from the $+X$ axis, and ϕ, measured in the Y–Z plane (counter-clockwise from $+Y$, so that $-Z$ is at $\phi = 90°$).

During ground calibration, an attempt was made to locate the X-ray optical axis by locating the peak of the effective area function as the HRMA was pitched and yawed. Measurements were taken for individual quadrants of the mirrors, with the aim of determining the mirror orientation for which the fluxes measured through diametrically opposed quadrants were the same. An internal misalignment of the HRMA optics resulted in an offset of $\sim 1'$ of that axis relative to the nominal mechanical axis as assessed optically by autocollimating off a reference flat (on the XRCF

Alignment Reference Mirror, or X-ARM) mounted within the HRMA. For most of the ground X-ray calibration, the zero reference for pitch and yaw was based on the optical measurements taken from the X-ARM.

During the analysis of the ground X-ray calibration data, it was found that the line profile (the point spread function [PSF] integrated over the Z direction) was broader than the raytrace model indicated. Better agreement would be obtained if the HRMA axis at zero pitch and yaw were actually at yaw $\sim -0.75'$, intermediate between the X-ray determined value (yaw $\sim -1'$) and the optically determined value for the optical axis location at zero pitch and yaw. Subsequently, detailed measurements of single-reflection ghosts relative to the direct images also suggested the presence of a bias in the zero point for pitch and yaw. The ghost images allow the magnitude of the off-axis angle to be accurately determined ($\lesssim 0'.05$), but the position angle is more difficult to assess; preliminary indications are that a yaw bias error of $\sim 0'.3 - 0'.6$ is likely.

The on-orbit optical axis determination was based on searching for a minimum in the PSF 50% and 90% encircled energy radii; because the focal surface curves towards the mirrors, the detector was placed slightly behind the on-axis focus (away from the HRMA). The star HR 1099 was imaged for a set 500 to 1000 second exposures using a corner of the HRC-I detector. The pointings were at $\theta = 0 - 4'$, with steps of $1'$, and at 8 position angles (ϕ) $45°$ apart. The 50% and 90% encircled energy radius was evaluated for each point (in sky coordinates), and the centroid of the (dithered) image was determined in "chip coordinates". The PSF width as a function of the two chip coordinates was fit by a symmetric quadratic function, yielding an estimate for the optical axis location; the optical axis was $\sim 20''$ from the prelaunch estimate, indicating there were no major shifts in the optical configuration as a result of launch. A more detailed analysis has been performed making use of the aspect system to take into account for any thermal or other effects which could shift the detectors relative to the HRMA (see Ref. 5).

4. SINGLE-REFLECTION GHOSTS

Single reflection ghost images occur when the photons reach the focal plane after missing either the paraboloid or the hyperboloid component of a given mirror pair. Photons which reflect off only a paraboloid component would focus at approximately twice the system focal length (if not intercepted by the H optic or a baffle), while photons which reflect off only a hyperboloid component focus (poorly) at about half the focal length (unless intercepted by a baffle). If only the P or H were present, then at the system (P + H) focal plane, the photons would form diffuse rings with radii about half of the optic radius. As sources move off-axis, these rings deform, forming a cardioid-like cusps when the off-axis angle is about the nominal graze angle for the optic, then forming portions of limaçon-like loops as the source moves further off-axis.

The HRMA was designed to suppress these single-reflection ghost images within a radius of $14'.6$ of the optical axis. In the cases of the outermost three mirror pairs (shells 1, 3, and 4), this was accomplished by adding tantalum baffles to the forwardmost baffle plate in the thermal precollimator, and to baffles placed at the aft face of the CAP (between the paraboloid and hyperboloid optics). For the smallest mirror pair, shell 6, baffles at these locations would not be sufficient to keep the central field clear of single-reflection ghosts, and in addition, a P_6 interior baffle was added to the design.

The ghosts predicted by the raytrace model were compared against those seen during the ground testing at the XRCF. In Fig. 1 we show an off-axis image including P_6 and H_6 single-reflection ghosts; the off-axis angle ($\sim 30'$) exceeds the nominal graze angle for the P_6H_6 optics, so the ghosts form loops passing through the direct image.

As noted in §3, in some cases the single-reflection ghosts can be used to assess the absolute off-axis angle. The dimensions of the ghost loops (*e.g.*, the azimuthal width of the H_6 ghost loop) and the relation of the ghosts to the direct image depend on the off-axis angle of the source direction relative to the optical axis. For the case shown in Fig. 1 (upper left), the best estimate of the off-axis angle based on the logs and the axial determination based on the ARM-X, was pitch $= -21'.240$, yaw $= 21'.214$, or $\theta = 30'.0195$, $\phi = -45°.0351$. (Here, pitch is a negative rotation about the $+Y$ axis, and yaw is a negative rotation about the $+Z$ axis.) A simulation using these values (Fig. 1, upper right) results in an H_6 ghost loop which is considerably narrower than that seen in the X-ray data. This indicates that the off-axis angle was actually somewhat larger. A better match is yielded by $\theta = 30'.303$; θ is probably within $\sim 0'.05$ of that value. The ϕ coordinate is less well constrained; it can be estimated by making use of the relations between the strut shadows and the image in both the direct image and in the ghost loops. It may be possible to estimate ϕ this to within $0'.1$ to $0'.2$. An effort is under way to reassess the HRMA optical axis location at XRCF by making use of the the full set of single-reflection ghost image data obtained during the ground calibration. Preliminary results indicate a yaw bias of $\sim -0'.25$ to $-0'.55$. Assessing the pitch bias is more difficult,

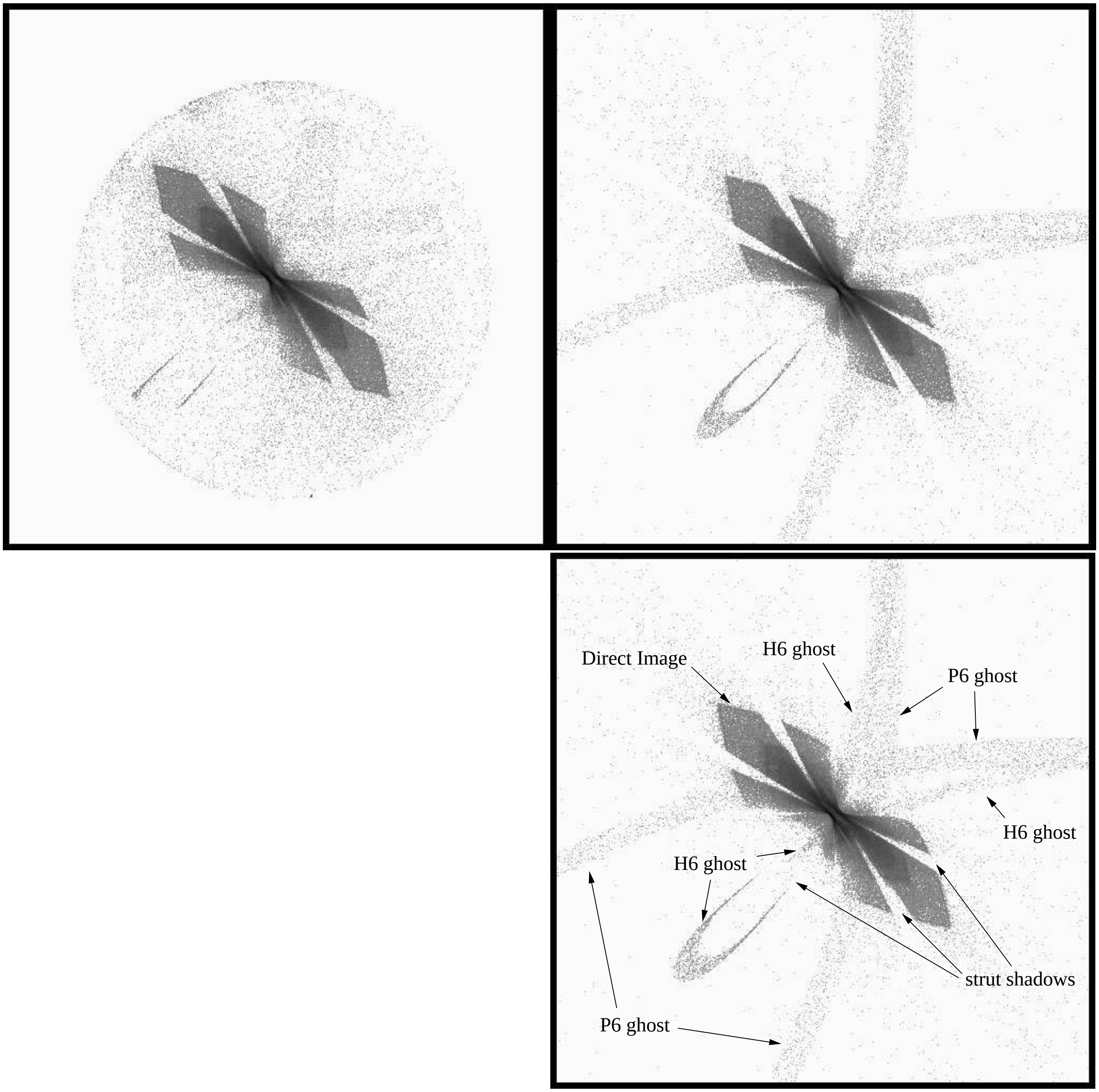

Figure 1. Off-axis single-reflection ghosts (ground calibration). Left: HSI image; Fe-K (E-IXH-PI-11.006, runid 110893). The planned angle was $\theta = 30'$, $\phi = -45°$; based on actuator readings and the assumed zero reference, the values were $\theta = 30.'0195$, $\phi = -45.^\circ0351$. The loop in the lower left is occulted by the HSI mask cusp. Right: Raytrace model using the nominal off-axis angle determined from the actuator readings and the assumed zero reference. Note that the H_6 ghost loop in the lower left is too narrow to match the observation, indicating that the source is really somewhat further off-axis. Bottom: Raytrace model better matching the observation; $\theta = 30.'3039$, $\phi = -44.^\circ75$). The ghost loops result from single-reflections off the P_6 or the H_6 optic; the gaps in the ghost loops are produced by the support strut shadows.

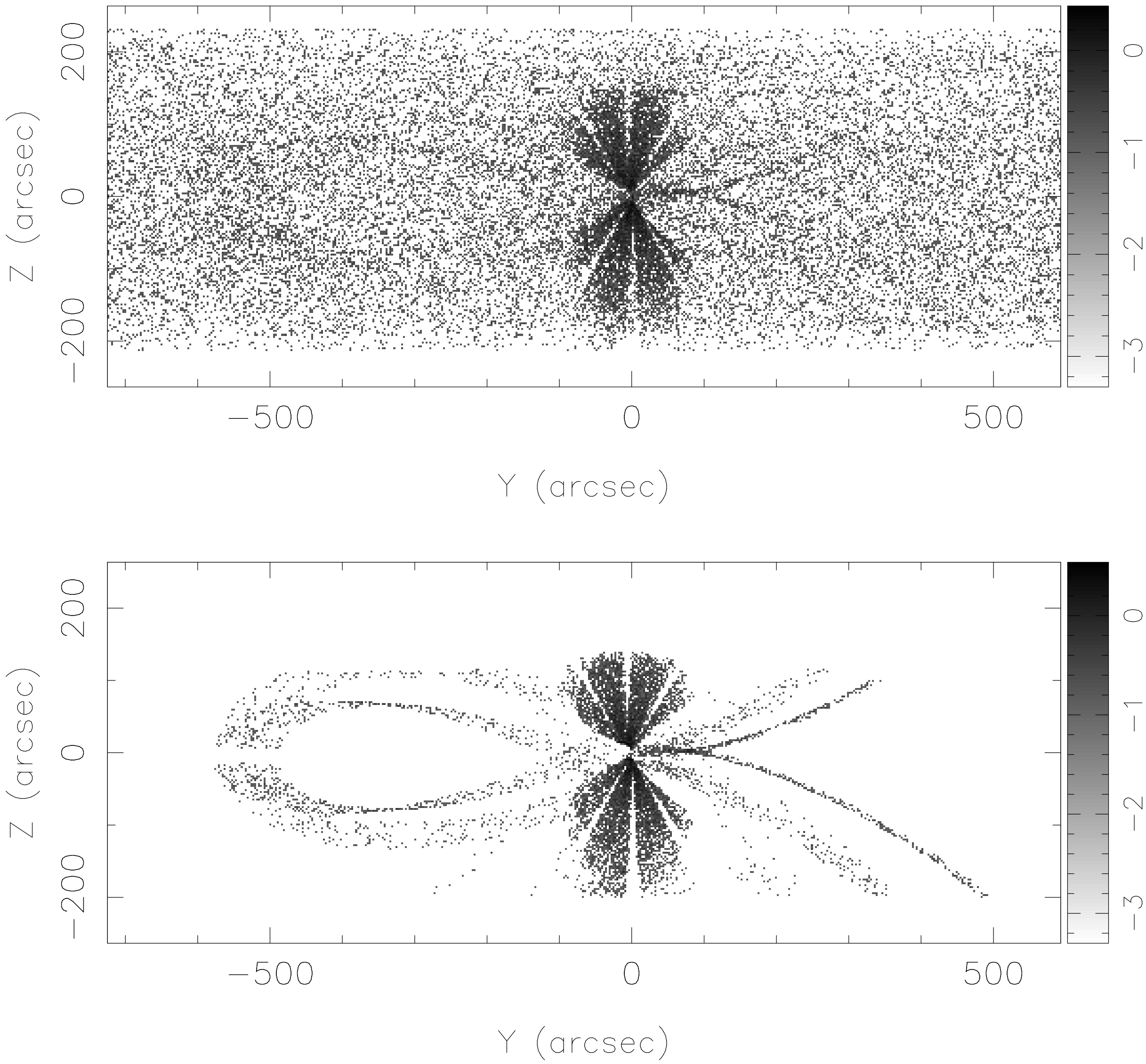

Figure 2. Off-axis single-reflection ghosts (on-orbit). Top: HRC-S image (obsid 1154); LMC-X1, offset 40′, 0′. Bottom: Raytrace model matching the observation; These ghost loops are a portion of a complex of single-reflection ghosts from the P_3, H_3, P_4, and H_4 optics; the P_6 and H_6 are too faint to be seen here and extend off the detector. In addition, there are P_1 and H_1 ghosts far to the right, well off the field of view of the detector.

but indications are that the pitch bias is $\lesssim 0'.2$ in magnitude. An accurate determination of the HRMA optical axis is important because it affects the determination of the mirror decenter/coma-compensated-tilt misalignment of the optics. This in turn affects the details of the off-axis imaging performance and also the asymmetric off-axis effective area.

So far, on-orbit data for single-reflection ghosts are scarce. The HRC-S detector samples furthest off-axis (though over a very narrow region) but the high background makes it difficult to see the fainter ghost features. In Fig. 2 we show an example of ghost images seen on-orbit using the HRC-S detector. In this case, both single-reflection P_4 and H_4 ghosts (forming faint cusps to the right of the direct image) and P_3 and H_3 ghosts (faint loops extending to the left) can be seen. Single reflection P_6 and H_6 (and P_1 and H_1 ghosts) can also be seen in the raytrace data prior to processing through `marx`, but these occur mainly outside the field of view of the detector.

5. OFF-AXIS IMAGING

As noted in §2, off-axis images were used to measure the internal coma-compensated decenter misalignments of the HRMA. The measurements at the XRCF were obtained at the nominal best focus location for the off-axis position, *i.e.*, the detector position followed the focal surface. In the XRCF images, a distinctive bright diamond-shaped feature can be seen in the core, particularly for moderate off-axis angles ($\lesssim 25'$) and lower energies. This feature (actually a superposition of four features, one for each mirror pair) is produced by the coma-compensated decenter of the optics.

On-orbit, the source LMC-X1 was observed at a number of locations for the purpose of determining plate scale. These images can also be used to examine the fidelity of the modeling of the HRMA misalignments. In Fig. 3, the data for obsids 1084 and 1069 are shown. For the simulations we used an LMC-X1 spectrum obtained by *ASCA*. The simulations contain approximately the same number of counts as the corresponding *Chandra* on-orbit images. Comparing the observations to the simulations, the agreement is good for the overall morphology. The core structure shows only one corner of the distinctive diamond pattern as part of an bright elongated oval feature; this is a consequence of the image being somewhat out of focus. The ACIS-S detector is designed to match the Rowland circle geometry for the gratings instead of the focal surface of the optics; at these far off-axis locations, the detector surface falls well behind the focal surface. When the image is defocused, the bright diamond features in the core unwrap, forming the oblong oval feature seen in the cores of the images. Sufficiently far out of focus, the unwrapping leads produces a hole in the center, and the image becomes a distorted ring. Note that in the obsid 1069 data, taken further off-axis (and further out of focus) shows a fainter region the core.

The surface brightness in the obsid 1084 data matches the raytrace reasonably well in the outer regions, but is clearly discrepant in the core: central $\sim 10''$ is considerably brighter in the simulation than in the actual observation. Detector pileup becomes significant for rates larger than ~ 0.1 cts pixel^{-1} frametime^{-1}. For obsid 1084, the raytrace predicts a peak of nearly ~ 0.6 cts pixel^{-1} frametime^{-1}, compared to a peak of ~ 0.3 cts pixel^{-1} frametime^{-1} in the X-ray data; the image core is heavily piled up in this case. The obsid 1069 exposure is further off-axis; the core is less piled up the core intensity agrees better with the raytrace prediction.

Qualitatively, the raytraces compare very well with the X-ray data. In detail, some differences can be seen; in the obsid 1069 data, the low intensity region in the core is somewhat larger in the X-ray data than in the raytrace. This suggests that the object was slightly further off-axis than indicated by the nominal offset, the focus was slightly off, or the mirror misalignment parameters are not quite right.

For an ideal perfectly-aligned HRMA, as the off-axis angle θ increases, the overall off-axis image size increases approximately quadratically with θ, becoming elongated in the azimuthal direction, but remaining symmetric about the plane containing the optical axis and the source direction. That is, for fixed off-axis angle θ and varying ϕ, the focal plane images are rotationally similar (neglecting support strut shadows), with image structure rotating directly with position angle ϕ. A consequence of the internal tilt-compensated decenters is additional image structure which rotates approximately as $\phi/2$. This can be seen in Fig. 3, in which the obsid 1084 and 1069 images are for sources differing $\sim 180^\circ$ in ϕ, but with obsid 1069 at slightly larger theta. Note that the bright elongated elliptical structure in the core of the image rotates approximately 90° between obsid 1084 and 1069; the perturbation of the outer edge also rotates only 90° compared to the $\sim 180^\circ$ rotation of the gross image structure. The obsid 1069 image is also ~ 1.7 times larger than the obsid 1084 image, consistent with its greater off-axis θ. Further details on the image asymmetries can be found in Ref. 4.

6. VIGNETTING

We define an energy-dependent *vignetting function*, V, as the effective area normalized to the on-axis effective area:

$$V_\Omega = \frac{A_{\mathit{eff},\Omega}(E,\theta,\phi)}{A_{\mathit{eff},\Omega}(E,0,0)}, \tag{1}$$

where Ω is the solid angle included in the effective area integral. Earlier estimates of the HRMA off-axis effective area were typically based on $\Omega = 2\pi$, *i.e.*, the effective area integrated over the full 2π sterad towards the detector plane. For source angles sufficiently far off-axis, the effective area sum includes singly-reflected ghost rays. The X-ray baffle design prevents ghost rays from intruding on the central $\sim 15'$ radius of the focal plane, and the

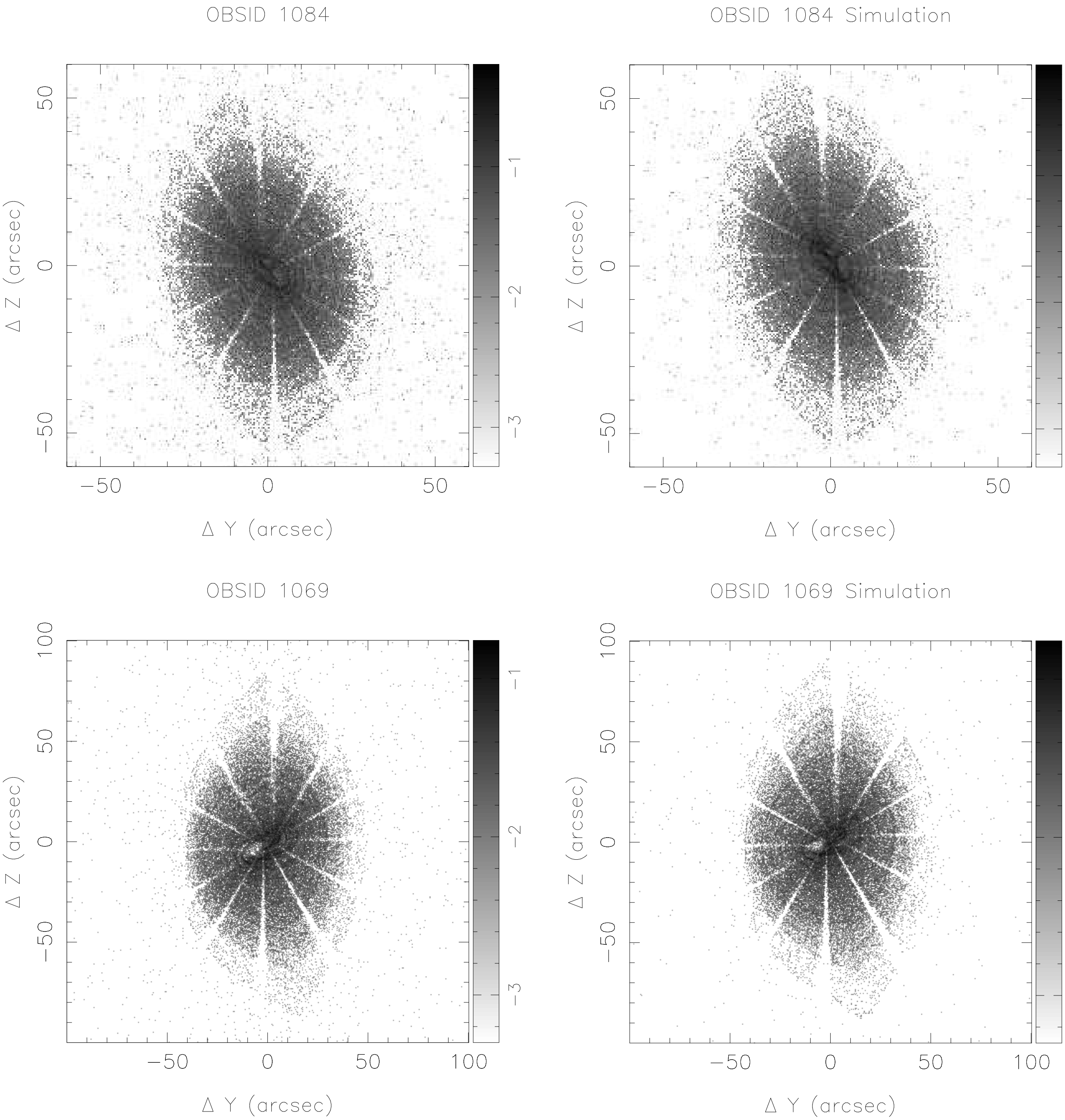

Figure 3. Off-axis PSF. The detector was 182 μm behind the nominal on-axis ACIS-S focus position. Top Left: ACIS-S image (obsid 1084). LMC-X1, offset $-16'.418$, $2'.366$; $\log_{10}$(counts/pixel/frame-time) is plotted. Top Right: ACIS-S image (simulation). LMC-X1, offset $-16'.418$, $2'.366$; $\log_{10}$(counts/pixel/frame-time) is plotted. Bottom Left: ACIS-S image (obsid 1069). LMC-X1, offset $20'.567$, $-1'.781$; $\log_{10}$(counts/pixel/frame-time) is plotted. Bottom Right: ACIS-S image (simulation). LMC-X1, offset $20'.567$, $-1'.781$; $\log_{10}$(counts/pixel/frame-time) is plotted.

thermal postcollimator in the aft HRMA structure removes ghost rays sufficiently far off-axis. Between these limits, single-reflection ghosts can get through. This is discussed further below.

The energy-dependent vignetting function depends on two factors: purely geometric vignetting, and mirror surface (reflectivity and scattering) properties. Purely geometric vignetting is determined by the geometry of the optics, baffles, and obstructions in the system. The reflectivity depends on the X-ray energy and the graze angle of the X-ray incident on the optic. For an ideal system, the graze angles for on-axis X-rays will vary slightly axially along the optic. For off-axis sources, the graze angle can vary strongly azimuthally around the optic; the most favorable and least favorable graze angles are in the plane containing the optical axis and the off-axis source direction. In the following, the term *vignetting* refers to the energy-dependent vignetting, i.e., the off-axis effective area normalized to the value at the optical axis.

In the zero-energy limit, reflectivity is near unity for a wide range of graze angles and the vignetting is almost entirely a result of the purely geometric vignetting. For clarity, consider a source moving off-axis upwards. Photons hitting near the top and near the bottom of the optic (*i.e.*, more or less in plane with the off-axis angle and the optical axis) increasingly miss one or the other optic and either run into baffles or reach the focal plane as single-reflection ghosts; near the sides the these are smaller effects. This is part of the reason that off-axis images become more compressed radially (and ultimately become bow-ties; see *e.g.* Fig. 1). The geometric area (and effective area) become increasingly dominated by the sides of the mirror perpendicular to the plane containing the source.

Furthermore, the graze-angles (and hence, reflectivity) vary markedly and systematically around the optic for off-axis sources. On the side of the optic closest to the source direction, the graze angles become shallower (increasing the reflectivity), and on the opposite side, the graze angles become steeper (decreasing the reflectivity). A photon hitting the P optic with shallow graze angle will, if it intercepts the H optic, tend to reflect from the H with a steeper graze angle, reducing the gain in reflectivity. In any case, the loss of geometric area due to geometric vignetting (eventually) overcomes any improvement in reflectivity in the plane containing the source. Near the sides, on the other hand, the variation in graze angle with source direction is much less extreme (a cosine effect), and the increasing concentration of geometric area towards the plane perpendicular to the source direction dominates the off-axis effective area. Thus, the dominance of the "sides" of the mirrors for larger off-axis angles results from a combination of retaining favorable graze angles and retaining geometric area.

Because the HRMA mirrors have differing nominal graze angles (ranging from $\sim 52'$ to $\sim 27'$), the vignetting function is strongly energy dependent. As noted above, the response at large off-axis angles is dominated by the "sides" of the optic where the graze angle is approximately the nominal graze angle. As the energy increases above the critical energy for the nominal graze angle for a given shell, the reflectivity drops rapidly and that shell becomes less and less important for the off-axis (and on-axis) effective area. This weights the vignetting function towards the smaller mirror pairs which have narrower geometric vignetting functions. This effect is clearly seen in Fig. 4 in which the vignetting function is plotted for a number of energies between ~ 0.01 and 10 keV. For energies up to ~ 3 keV, the vignetting function is relatively insensitive to energy as can be seen by the close spacing of the curves in Fig. 4. From ~ 3 to ~ 7 keV, the off-axis effective area falls rapidly, while near 8 keV, the energy dependence flattens out or even reverses.

Because of the internal misalignment (coma-compensated decenter) within the HRMA, the off-axis response is asymmetric. This shows up clearly in the off-axis PSF (see Ref. 4, where this fact was used to diagnose and quantify the internal misalignment parameters). This also has implications for the off-axis vignetting behavior. In Fig. 4 note that the peak of the vignetting function is $\sim 1-2'$ off axis (most noticeable at lowest energies).

In Fig. 5 we plot vignetting functions $V_\Omega(E,\theta,\phi) = A_{\mathit{eff},\Omega}(E,\theta,\phi)/A_{\mathit{eff},\Omega}(E,0,0)$ as a function of ϕ for four energies. Consider first the upper curve for each energy; these are evaluated for $\Omega = 2\pi$. The approximately sinusoidal variation is a consequence of the internal tilt-compensated decenter misalignment of the HRMA. The amplitude the variation with ϕ decreases for increasing energy, but the relative variation is fairly constant, with peak the peak exceeding the valley by ~ 7 or 8% for $\theta = 15'$. In the 9.5 keV case, the response with ϕ is also modulated with a cycle of 30°; this is a result of the shadows produced by the support struts, located every 30° from $\phi = 0°$.

In Fig. 5 the lower curve for each energy shows the result of evaluating the effective area over a rectangle corresponding to the HRC-I detector. At $\theta = 15'$, the source falls at or near the edge of the detector at $\phi = 45°$, 135°, 225°, and 315°; this produces the notches at those values of ϕ. Overall, away from these angles, there is a net depression in the vignetting function relative to the $\Omega = 2\pi$ vignetting function. This is a result of single reflection ghosts extending well beyond the edge of the detector, which are included in the $\Omega = 2\pi$ sum. In Fig. 5, the $\Omega = 2\pi$

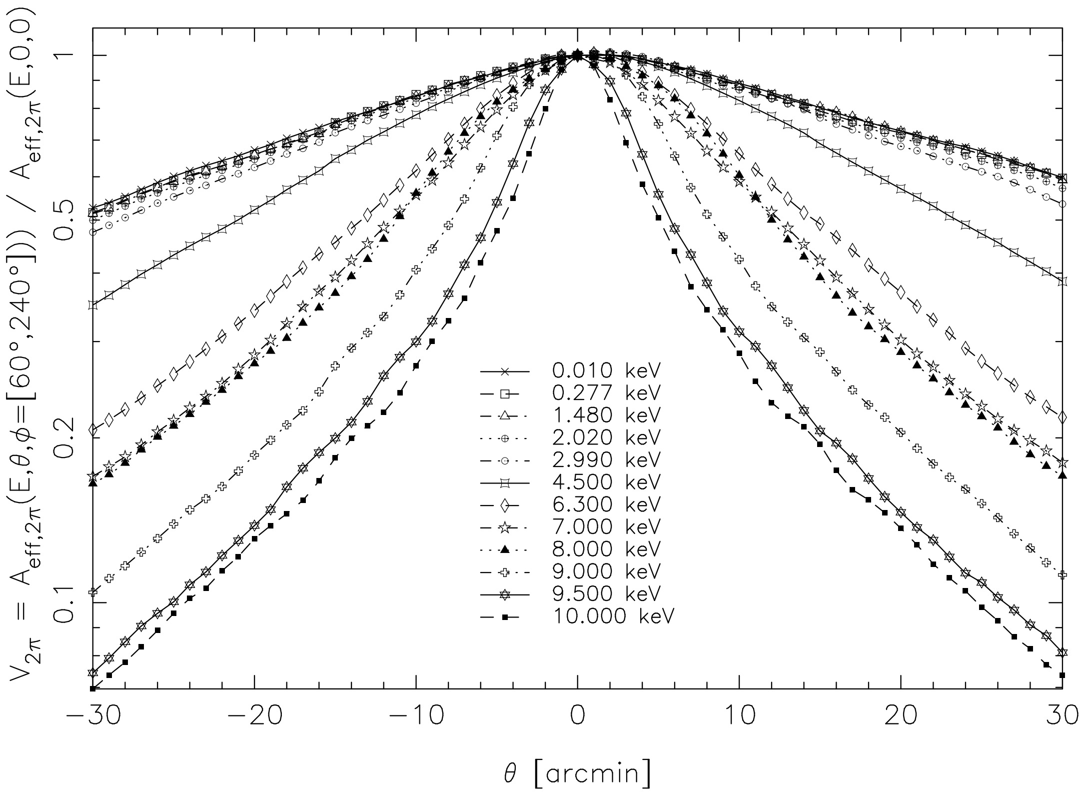

Figure 4. Energy-dependent vignetting as a function of angle for a number of energies. This is a slice taken approximately through the axis of greatest asymmetry.

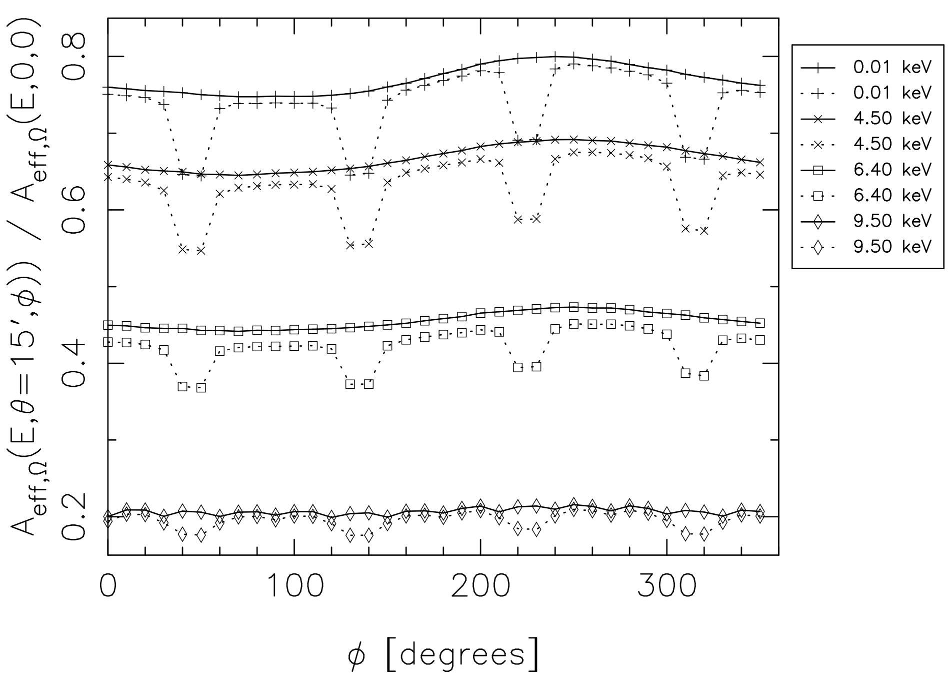

Figure 5. Energy-dependent vignetting for $\theta = 15'$ as a function of ϕ for 4 energies. The top curve for each energy shows $A_{eff,\Omega=2\pi}(E,\theta,\phi)/A_{eff,\Omega=2\pi}(E,0,0)$, while the lower curves show the effect of clipping by a square corresponding to the HRC-I clear aperture.

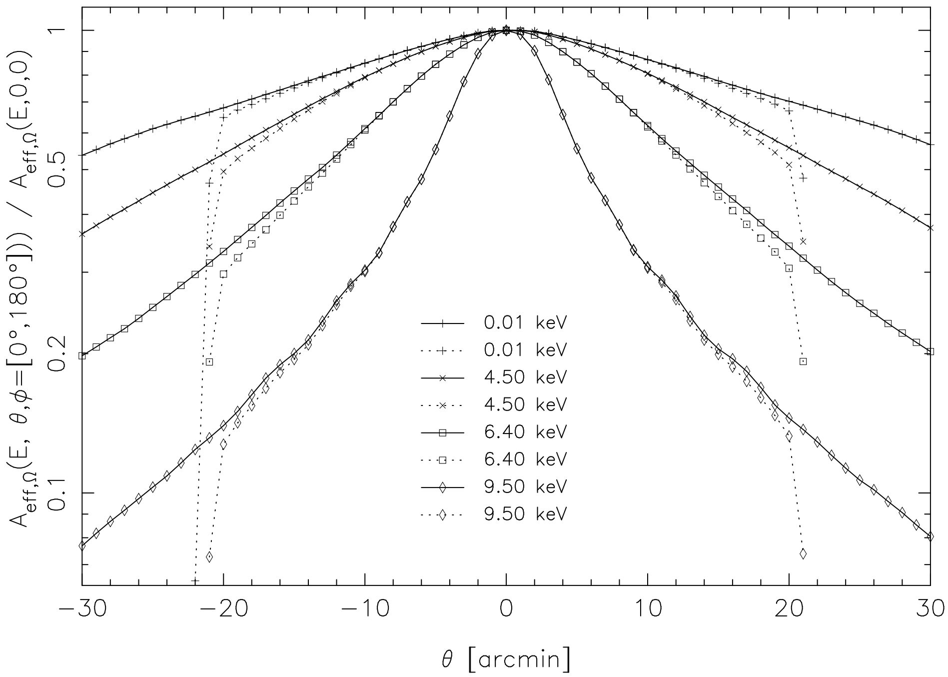

Figure 6. Effect of single-reflection ghosts on vignetting calculation. The solid curves represent $V_{\Omega=2\pi}$, while the dashed curves show V_{Ω} for a region corresponding to the extent of the HRC-I detector. The is a slice for $\phi = 0°$ and $\phi = 180°$.

case overestimates the vignetting by up to $\sim 5\%$ for $\theta = 15'$. Finally, in Fig. 6, we show the vignetting function for a slice with $\phi = 0°$ and $\phi = 180°$, aligned with one of the long axes of the HRC-I detector. In these directions, the direct source image falls off the detector at $\sim 21'$ off-axis; the effective area sum falls rapidly for $\theta > 20'$ as the direct image and single-reflection ghosts are increasingly vignetted by the detector edge. It can also be seen that $V_{2\pi}$ overestimates the detector-specific HRMA vignetting function by as much as 10%. It is evident that HRMA vignetting functions tailored to each detector geometry will be needed.

In order to assess the off-axis effective area on orbit, the supernova remnants G21.5-0.9 and Cassiopeia A (Cas A) were observed on each ACIS chip; both sources peak in intensity around 2 keV. In the following we present a preliminary comparisons of the G21.5-0.9 data to the raytrace model. The effective areas were based on (background subtracted) count rates and photon spectra for the for the portion of the central core of the remnant imaged within a single node of the chip. The off-axis effective areas for the HRMA model were obtained by using off-axis effective areas calculated on a coarse angular and energy grid to rescale the on-axis effective area, computed on a much finer energy grid. Note that these HRMA effective areas are all 2π effective areas, not taking into account the vignetting of ghosts by the detector edges. The model off-axis effective area was multiplied by the ACIS quantum efficiency (QE) averaged over the chip to obtain the combined model HRMA plus ACIS effective area. (For S1 and S3, a correction factor was also applied for variation of QE over the chip.) In Fig. 7 we plot the results for 4 off-axis angles (approximately along $\phi = 180$ deg for S0, S1, and S2, $\phi = 0°$ for S5). Qualitatively, the agreement is reasonably good; below ~ 1 keV and above ~ 7 keV, the source strength and effective areas are very low and the data are unreliable. Further analysis (*e.g.*, the effects of ghost vignetting by the detector) is needed before meaningful constraints on the HRMA model can be extracted.

7. CONCLUSIONS

The calibration raytrace model agrees well qualitatively for the off-axis imaging performance and the off-axis ghost predictions. In detail, differences appear. The on-orbit data will be combined with reanalysis of the ground calibration data to refine the mirror alignment model. The on-orbit data have better determinations of source angle but poorer separation of individual mirror effects. The ground data provide information on individual mirror pairs, but currently

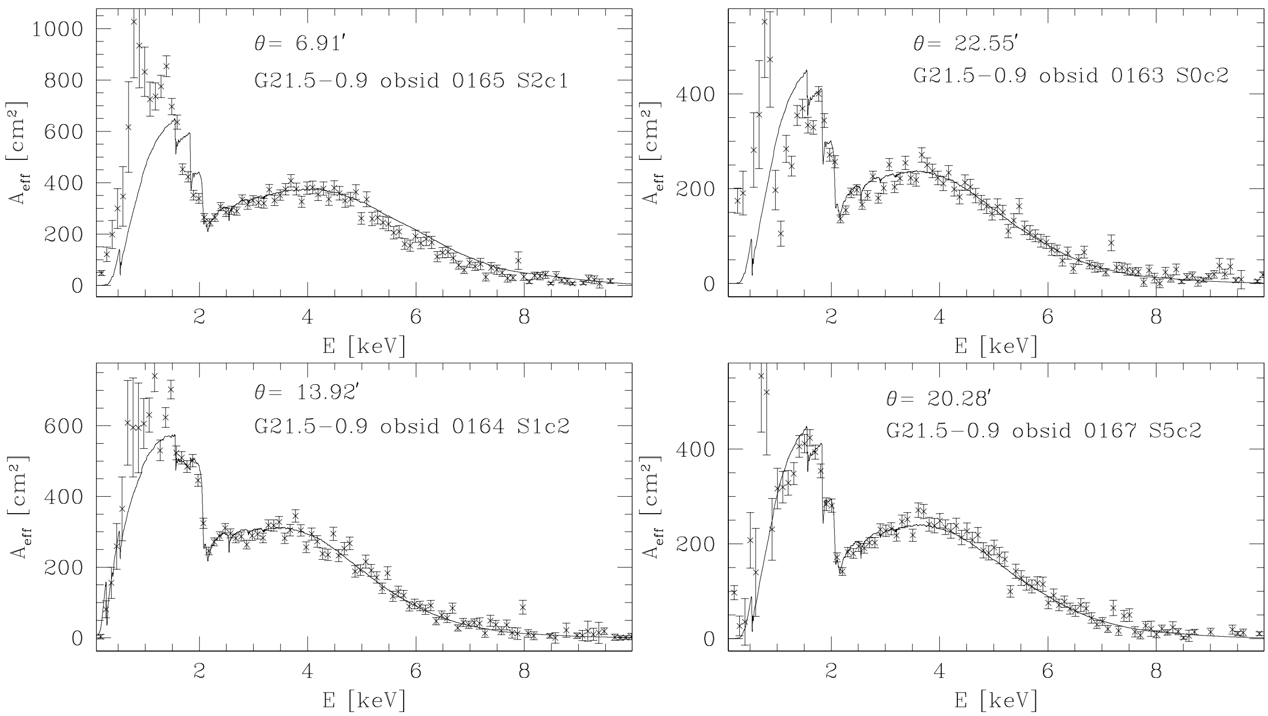

Figure 7. Off-axis Effective Area obtained from on-orbit observation of G21.5-0.9. Top Left: ACIS-S2, node 1; $\theta = 6.'91$. Top Right: ACIS-S1, node 2; $\theta = 13.'92$. Bottom Left : ACIS-S0, node 2; $\theta = 22.'55$. Bottom Right: ACIS-S5, node 2; $\theta = 20.'28$.

suffer from an uncertainty in the location of the optical axis; the optical axis determination will be refined making use of measurements based on single-reflection ghost positions.

The model vignetting response is asymmetric, depending on energy and both off-axis angles. Furthermore, the single-reflection ghosts extend over large regions of the focal plane; vignetting functions tailored to the geometric dimensions of each detector will be more appropriate than functions summing the effective area over the full 2π steradians. Preliminary analyses of the on-orbit data for off-axis effective area compared to the $\Omega = 2\pi$ effective areas show reasonable agreement for the range of energies corresponding to the dominant X-ray energies in the sources. However, the on-orbit vignetting data and the raytrace model are not yet sufficiently well understood to constrain the raytrace model; work will continue on refining our understanding of the model and of the on-orbit performance.

ACKNOWLEDGMENTS

This work was supported by NASA contract NAS8-39073.

REFERENCES

1. M. C. Weisskopf and S. L. O'Dell, "Calibration of the axaf observatory: overview," in *Grazing Incidence and Multilayer X-Ray Optical Systems*, R. B. Hoover and A. B. C. W. II, eds., *Proc. SPIE* **3113**, pp. 2–17, 1997.
2. D. E. Graessle, A. J. Burek, J. J. Fitch, B. Harris, and D. A. Schwartz, "Optical constants from synchrotron reflectance measurements of the axaf witness mirrors 2 to 12 kev," in *Grazing Incidence and Multilayer X-Ray Optical Systems*, R. B. Hoover and A. B. C. W. II, eds., *Proc. SPIE* **3113**, pp. 52–64, 1997.
3. M. W. Wise, J. E. Davis, D. P. Huenemoerder, J. C. Houck, D. Dewey, K. A. Flanagan, and C. Baluta, *The MARX 2.0 User Guide*, AXAF Science Center, 1997.
4. T. J. Gaetz, W. A. Podgorski, L. M. Cohen, M. D. Freeman, R. J. Edgar, D. Jerius, L. V. Speybroeck, P. Zhao, J. Kolodziejczak, and M. Weisskopf, "Focus and alignment of the axaf optics," in *Grazing Incidence and Multilayer X-Ray Optical Systems*, R. B. Hoover and A. B. C. W. II, eds., *Proc. SPIE* **3113**, pp. 77–88, 1997.

5. J. McDowell, “Coordinate systems for analysis of on-orbit Chandra data. Paper I: Imaging,” *in preparation* , 2000.